



Indre Joedicke · Naeim Ghavidelnia · Gerrit Felsch ·
Viacheslav Slesarenko 

Addressing manufacturing defects in architected materials via anisotropy: minimal viable case

Received: 18 July 2023 / Revised: 21 December 2023 / Accepted: 7 January 2024
© The Author(s) 2024

Abstract The emergence of additive manufacturing has enabled the fabrication of architected materials with intricate micro- and nanoscale features. However, each fabrication method has a specific minimum feature size that can be practically achieved. As engineers pursue lightweight and high-performance materials, the elements of these architected materials often approach this minimum feature size, which poses a risk to their structural integrity. The failure of individual struts can result in the complete breaking of the lattice metamaterial's connectivity or, depending on the internal architecture, only a marginal reduction in its load-bearing capacity. In this short letter, we use a minimal viable unit cell to demonstrate how an anisotropic lattice, constructed with beams of varying thicknesses, can surpass a lattice consisting solely of uniform thickness beams in terms of damage tolerance. Our focus is primarily on the manufacturing limitations rather than defects that may arise during the loading of architected materials. We propose an approach where the probability of each individual strut failure depends on its thickness, and we illustrate the implications using a simple step-like function. This approach can be extended to more complex metamaterials or to explore intricate relationships between failure probability and beam thickness.

1 Introduction

Architected materials leverage intricate structure-properties relationships to exhibit unconventional combinations of properties [1–3]. The most prevalent type of architected materials comprises lattice-based structures, which are constructed by slender struts connected at nodes, resulting in periodic arrangements [4–6]. In addition to their extremely high stiffness [1], these materials can exhibit remarkable mechanical phenomena, including negative Poisson's ratio [7–9] and negative thermal expansion [10]. From a mechanical perspective, their rational design allows for the realization of various stiffness tensors in both 2D and 3D settings [11], enabling, for instance, unusual coupling between compression deformation and twist [12, 13].

To assess the effective stiffness tensor of architected materials, various homogenization techniques have been employed [14–16]. However, when transitioning from architected metamaterials characterized by a single repeating unit cell in two or three dimensions to heterogeneous metamaterials composed of unit cells with diverse local geometries, alternative techniques need to be implemented [17–20], often relying on deep learning approaches [21–23]. Heterogeneous metamaterials have the potential to offer advantageous properties, such as toughness [24], resilience [25], plastic energy absorption [26], or damage tolerance [27, 28].

I. Joedicke · N. Ghavidelnia · G. Felsch · V. Slesarenko (✉)
Cluster of Excellence livMatS @ FIT – Freiburg Center for Interactive Materials and Bioinspired Technologies, University of Freiburg, Georges-Köhler-Allee 105, 79110 Freiburg, Germany
E-mail: viacheslav.slesarenko@livmats.uni-freiburg.de

I. Joedicke · N. Ghavidelnia · G. Felsch · V. Slesarenko
Department of Microsystems Engineering, University of Freiburg, Georges-Köhler-Allee 103, 79110 Freiburg, Germany

The growing interest in architected lattice-based materials is inseparable from advancements in manufacturing techniques. Notable examples of real-life metamaterials from 2012 [29] and 2016 [30] were fabricated using additive manufacturing (AM). The continuously expanding array of AM methods for architected materials [31, 32] spans from macroscopic fused filament fabrication (FFF) [33] and stereolithography (SLA) [34] to more precise techniques like two-photon polymerization [29] and AM-pyrolysis combinations [35, 36]. Simultaneously, the reduction in feature size to the microscopic and nanoscopic scales enables the realization of mechanical behavior that would be nearly impossible at larger scales. In particular, in nano- and micro-lattices, since the second moment of inertia scales with the fourth power of the linear size, struts can undergo significant bending without failure. This aspect is especially significant for metallic metamaterials, given their relatively low strain to yielding [37]. Moreover, fabricating at the nanoscale allows for defect-free elements, making metamaterials virtually immune to flaws [30]. At the same time, there is a certain compromise that needs to be made. While smaller features can lead to enhanced properties, their manufacturing becomes less certain and robust. Consequently, if the minimum feature size approaches the limits of the selected fabrication method, certain elements of the architected materials may be susceptible to failure due to manufacturing issues [32], potentially compromising the overall performance of the architected material [31].

Traditionally, the robustness of metamaterials has been associated with their ability to withstand damage and maintain their properties under loading conditions [25, 27]. However, in this study, we aim to investigate the reliability of architected materials by specifically focusing on scenarios where certain struts are initially compromised due to fabrication at the limits of the chosen manufacturing process. Several existing works have explored the behavior of lattices with potential manufacturing imperfections [38] or when some struts are missing from the outset [23]. In this study, we concentrate on anisotropic triangular-based lattices with the minimum viable configuration, assuming that the survival of each individual strut during fabrication depends on its thickness. The objective of this concise letter is to propose an approach for addressing the robustness of lattices composed of elements with thicknesses close to the manufacturing limits.

2 Method

To illustrate our approach, we selected the minimal viable scenario, which involves an equilateral-triangular lattice defined by the thickness of three beams comprising the unit cell, as depicted in Fig. 1. The unit cell is repeated periodically along vectors e_1 and e_2 to form the entire lattice. In this lattice configuration, the removal of any one of the three beams does not result in a loss of topological connectivity. However, it is evident that the compromise of a single beam within this unit cell would impact the effective stiffness matrix.

In contrast to classical well-studied lattices where all three beams (0, 1, 2) in the unit cell have the same thickness, the lattices analyzed in this letter consist of beams with varying thicknesses. While equi-thickness lattices can be classified as isotropic [39], it is evident that this is not the case for the lattices defined by the unit cells shown in Fig. 1b. We note that the claim about the isotropy of the equi-thickness lattice is made under the assumption of the classical Cauchy continuum model, which we adopt hereinafter. Higher-order theories, taking into account, for instance, strain gradients, might introduce additional size effects in the considered lattice systems [40–42].

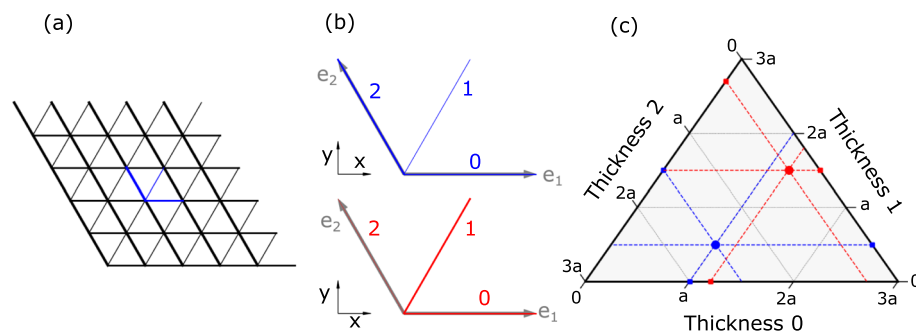


Fig. 1 **a** Example of a lattice. **b** Two unit cells with numbered beams. The Cartesian coordinate system is shown in black and the local coordinate system in grey. **c** Position of unit cells from **(b)** in a ternary plot of the design space. a designates the average beam thickness

An important characteristic of the lattice is its effective density, and in optimization processes, it is often desirable to maintain a constant density throughout the lattice, as observed in studies such as [43,44]. Given that the beams have the same out-of-plane thickness and are made of the same material, we explore different unit cells with the same density by imposing a constraint on the average beam thickness a . Consequently, for each generated unit cell, we have three variables (thicknesses) with a fixed average. The ternary plot [45] displayed in Fig. 1c provides a clear visualization of the design space. Each point inside the triangle corresponds to a feasible lattice configuration, and the associated beam thicknesses can be determined by plotting three straight lines parallel to the sides of the triangle and passing through the selected point.

To understand the behavior of the considered lattices and analyze their sensitivity to partial failure, it is essential to comprehensively explore the entire design space through experiments or simulations. However, as the number of variables (beams) increases, the design space expands rapidly, which is why this letter focuses on the minimal feasible design. If we allow for N possible thicknesses for each beam in the unit cell, the total number of potential unit cells of the same mass will be $N(N + 1)/2$. However, if we consider a new unit cell consisting of four smaller ones, the number of independently defined beams increases to 12, resulting in a total number of valid lattices approximating $(N + 10)! / [(N - 1)! \cdot 11!] \approx 4 \cdot 10^{14}$ for $N = 100$, making systematic analysis infeasible. Furthermore, if the beam thicknesses are chosen randomly, the problem becomes even more challenging. In such cases, a larger unit cell provides a higher probability of obtaining configurations with "average" properties, leaving a substantial portion of the design space unexplored. Consequently, exploring the design space becomes a problem that goes beyond purely mechanical considerations and falls within the domain of active learning. Techniques such as Bayesian optimization can be employed to address this challenge [23].

To map the design and property spaces, we utilized LatticeMech code [46]. The computational scheme of LatticeMech is based on the Euler–Bernoulli beam model, assuming small strains and employing an asymptotic expansion of the kinematic and static variables (for further details, refer to [47,48]). In order to maintain constant density, we set the sum of all beam thicknesses equal to $3a$, where a represents the average thickness of the beams. Simultaneously, to satisfy Euler–Bernoulli conditions, the lengths of all beams were fixed at $10a$. Our calculations yield the complete stiffness tensor \mathbf{S} , which comprises six independent entries for the 2D case. As a result, we establish a mapping between three variables (thicknesses) in the geometry domain and six variables in the property domain. To reduce the number of variables in the property domain, one approach is to introduce a measure for the anisotropy of the material as an effective characteristic of the stiffness tensor. Commonly used measures of anisotropy include the Zener ratio [49,50] and the universal anisotropy index [51]. These metrics are initially designed for 3D crystals, and adapting them to non-orthotropic or 2D structures is not straightforward [52]. Therefore we introduce an anisotropy coefficient ξ following the approach of Mendez et al. [53]. This coefficient quantifies the deviation from an isotropic reference tensor \mathbf{S}_{iso} :

$$\xi = \|\mathbf{S} - \mathbf{S}_{iso}\|, \quad (1)$$

where $\|\cdot\|$ denotes a suitable matrix norm. The anisotropy coefficient ξ provides a concise representation of the anisotropy of the stiffness tensor, enabling a reduction of the property domain variables while capturing the essential information related to the material behavior. An isotropic stiffness tensor must be defined by:

$$\begin{aligned} S_{iso,xxxx} &= S_{iso,yyyy} = 2\mu_{iso} + \lambda_{iso} \\ S_{iso,xyxy} &= 2\mu_{iso} \\ S_{iso,xxyy} &= S_{iso,yyxx} = \lambda_{iso} \\ S_{iso,xxxy} &= S_{iso,yyxy} = S_{iso,xyxx} = S_{iso,xyyy} = 0, \end{aligned} \quad (2)$$

where λ and μ are Lamé constants. To relate current tensor to the closest isotropic materials, we choose μ_{iso} so that $S_{xyxy} = S_{iso,xyxy}$ and λ_{iso} so that the error for S_{xxxx} and S_{yyyy} is minimized, i.e.

$$\begin{aligned} \mu_{iso} &= \frac{S_{xyxy}}{2} \\ \lambda_{iso} &= \frac{S_{xxxx} + S_{yyyy}}{2} - 2\mu_{iso} \end{aligned} \quad (3)$$

3 Results and discussion

By systematically exploring the design space for three-beam unit cells, we can uncover relationships between different components of the stiffness tensor, as depicted in Fig. 2a, b. Taking the stress tensor component S_{xxxx} as the reference, Fig. 2a, b illustrate the possible values of the other components, namely S_{yyyy} and S_{xxyy} . It is evident that the stiffnesses in the x and y directions (S_{xxxx} and S_{yyyy}) are tightly interconnected, allowing only specific linear combinations. This linear dependency in relation to S_{xxxx} is also observed for the other two components of the stiffness tensor, S_{xyxy} and S_{xxyy} . This observation stems from the condition of mass conservation within the lattice. On the other hand, a wider range of combinations is admissible for S_{xxyy} and S_{xyxy} (Fig. 2b). It is noteworthy that in all the presented plots, the extreme points in the property domain correspond to extreme points in the geometry domain. For example, in Fig. 2g, the fourth unit cell exhibits the combination of the minimal possible S_{yyyy} stiffness and the maximal S_{xxxx} stiffness due to the concentration of mass in the horizontal beam (beam 0). This relationship highlights the direct correspondence between the geometric arrangement of the unit cell and the resulting stiffness properties.

Ternary plots provide a more direct visualization of the connection between the geometric and property domains, as demonstrated in Fig. 2c, d. The noticeable symmetry arises from the orientation of the unit cell relative to the coordinate system, where beam 0 aligns with the x-direction, while beams 1 and 2 do not (Fig. 1b). An increase in the thickness of horizontal beam 0, accompanied by a decrease in the thicknesses of the other two beams, results in an growth of S_{xxxx} and a drop of S_{yyyy} . A more informative comparison can be made by examining the effective geometrical factor and effective property, as depicted in Fig. 2e, f. Figure 2e shows the purely geometrical variance in beam thickness, calculated as the standard deviation of the beam thicknesses using the formula $\sqrt{1/3 \sum_{i=0}^2 (t_i - a)^2}$, where t_i represents the thickness of the i-th beam. Figure 2f presents the anisotropy coefficient ξ calculated using Eq. (1). Notably, there are qualitatively similar dependencies of variance and anisotropy coefficient on beam thicknesses. In the center point corresponding to the equi-thickness lattice, the stiffness tensor is isotropic. As we move toward the sides of the triangle, both the variance and anisotropy coefficient increase simultaneously. These findings are consistent with previous studies on triangular lattice materials [39].

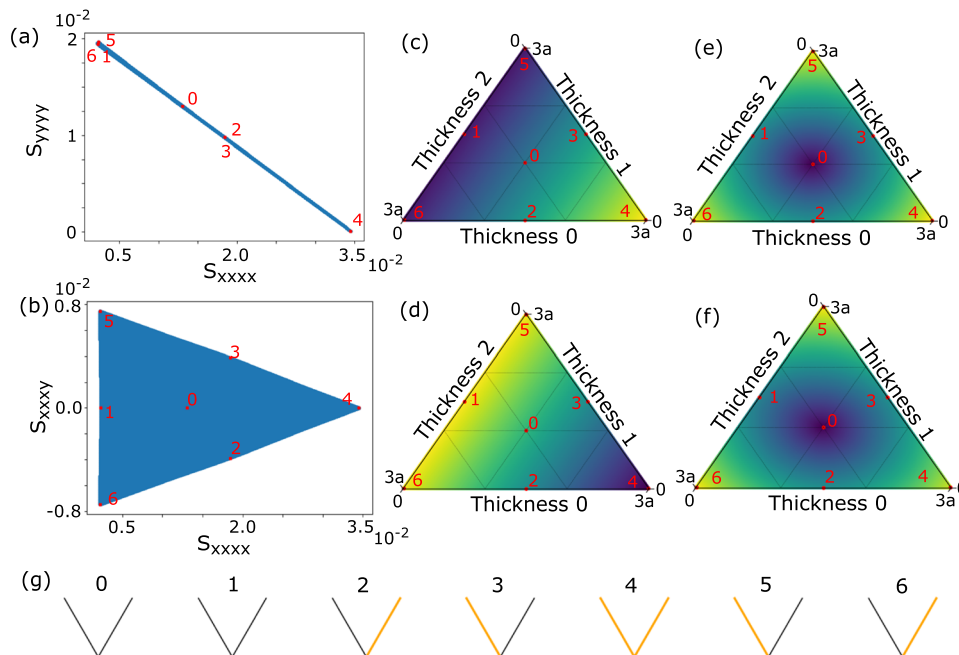


Fig. 2 Design space without failure. **a** and **b** Stiffness S distributions. **c** and **d** Ternary plots for S_{xxxx} and S_{yyyy} components. **e** Ternary plot for standard deviation of the beam thicknesses. **f** Ternary plot for anisotropy coefficient ξ . Note that for **c–f**, the color represents just qualitative dependencies and color range might have different minimal and maximal values for each plot. **g** Unit cells for special cases. An orange line represents a beam with a thickness close to 0. In **(a–f)** the special lattices are represented by red dots

The analysis of intact lattices provides valuable insights into the relationship between the design space and property space. However, it does not impose any restrictions on the minimum thickness of individual beams. In reality, every fabrication process has a minimum feature size that sets limits on the range of feasible lattices that can be manufactured. Moreover, even features with dimensions close to this critical threshold size may be vulnerable to damage during fabrication. In our proposed approaches, we account for this by assuming a specific relationship between the feature size (beam thickness t) and the probability of failure P . For illustrative purposes in this communication, we explore the consequences of this approach using a relatively simple step-like function shown in Fig. 3a, defined as:

$$P(t) = \begin{cases} 0\% & \text{if } t \geq t_{\text{th}} \\ 100\% & \text{else} \end{cases} \quad (4)$$

where t_{th} represents the critical minimum thickness. According to this function, if the beam thickness is equal to or greater than the critical threshold, the probability of failure is 0%. Otherwise, if the beam thickness is below the critical threshold, the probability of failure is 100%. Failed beams are modeled with a thickness of 0, which means they do not contribute to the material stiffness in the case of failure. For each lattice, we can distinguish between three cases. In the first case, none of the beams fail and the lattice remains intact. Alternatively, the lattice can fail completely, i.e. so many beams fail that the lattice gets disconnected. Finally, the lattice can fail partially but remain topologically connected still maintaining some load-bearing capacity. For the selected failure probability function, the relation between average beam thickness a and critical size t_{th} plays a core role, as shown in Fig. 3.

Figure 3c, d illustrates the positions of intact, completely failed, and partially failed lattices in a ternary plot for two different cases ($a > t_{\text{th}}$ and $a < t_{\text{th}}$). We observe that when the threshold t_{th} is smaller than the average beam thickness a , there is a central region in the ternary plot corresponding to intact lattices. This region represents unit cells with almost identical beam thicknesses. At the corners of the plot, there are three distinct regions of complete failure, indicating the failure of two beams. The three separate regions of partial failure are located at the midpoint of each side, representing the failure of only a single beam. On the other hand, when the threshold t_{th} is equal to or larger than a , there are no intact lattices in the design space since, by definition, all beams cannot be simultaneously thicker than the average beam thickness a . Instead, an additional region of complete failure emerges in the central area of the ternary plot, where all beams fail. However, the regions of partial failure still persist even when the threshold is larger than a .

The ternary plots also allow us to determine the relative ratios of intact, partially failed, and completely failed lattices based on simple geometric considerations. The relative number of lattices in each group for a fixed average beam thickness a is a function of the threshold t_{th} . The areas of the regions corresponding to intact, completely failed, and partially failed lattices can be expressed as follows:

$$\begin{aligned} A_{\text{intact}}(t_{\text{th}}) &= \begin{cases} \frac{1}{9a^2} (3a - 3t_{\text{th}})^2 & t_{\text{th}} \leq a \\ 0 & a \leq t_{\text{th}} \leq \frac{3}{2}a \end{cases} \\ A_{\text{complete}}(t_{\text{th}}) &= \begin{cases} \frac{2}{3a^2} t_{\text{th}}^2 & t_{\text{th}} \leq a \\ \frac{2}{3a^2} (-3a^2 + 6at_{\text{th}} - 2t_{\text{th}}^2) & a \leq t_{\text{th}} \leq \frac{3}{2}a \end{cases} \\ A_{\text{partial}}(t_{\text{th}}) &= \begin{cases} \frac{1}{3a^2} t_{\text{th}} (6a - 5t_{\text{th}}) & t_{\text{th}} \leq a \\ \frac{1}{3a^2} (3a - 2t_{\text{th}})^2 & a \leq t_{\text{th}} \leq \frac{3}{2}a \end{cases} \end{aligned} \quad (5)$$

Figure 3b illustrates the ratios between size of three above-mentioned group as a function of threshold value t_{th} derived from simulations. Identical values were obtained from Eq. (5). This figure shows that the higher the threshold the larger percentage of lattices that fail completely, reaching 100% for $t_{\text{th}} = 1.5a$ when all lattices fail. In contrast, the number of lattices that remain intact (no failure at all) gradually decreases with an increase of t_{th} , and for $t_{\text{th}} > a$, all lattices have at least one failing beam. However, quite non-orthodox dependency can be traced by observing lattices that partially failed. The number of such lattices monotonically increases for relatively small values of t_{th} , however starts to decline after peaking for $t_{\text{th}} = 3/5a$. This value can be derived directly by taking the derivative of Eq. (5).

It is clear that the introduction of probable failure does not affect the mechanical properties of the lattices that remain intact. Simultaneously, lattices that fail completely lose any load-bearing capacity. Therefore, the main interest lies in partially failed lattices that still retain reasonable stiffness, although not identical to the

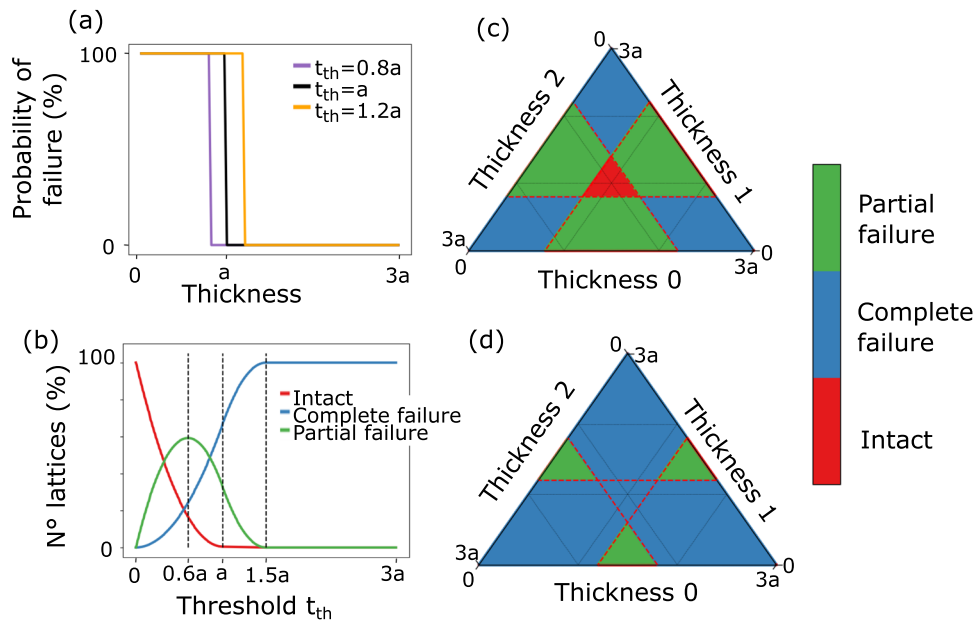


Fig. 3 **a** Function $P(t)$ describing the probability of failure. **b** Influence of the threshold on the number of lattices in the different groups. **c** and **d** Location of the lattices from three different classes on ternary plot for $t_{th} < a$ (**c**) and $t_{th} > a$ (**d**)

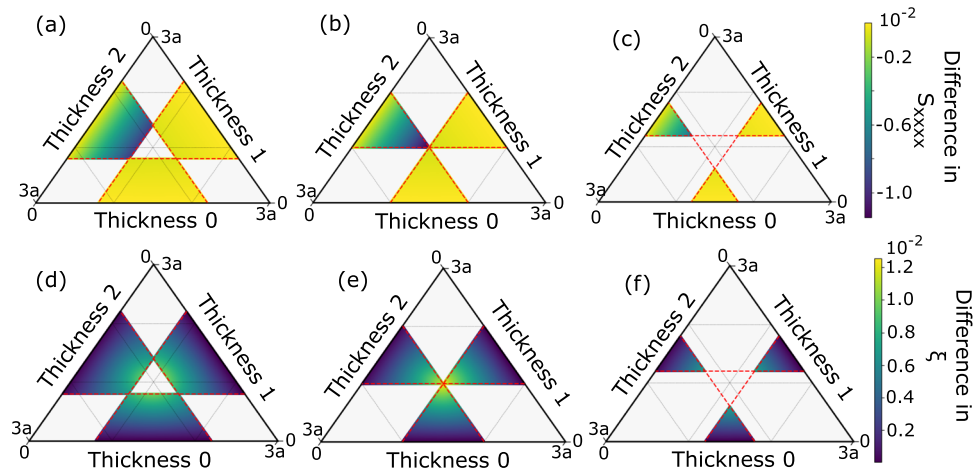


Fig. 4 Change of stiffness component S_{xxxx} (**a-c**) and anisotropy coefficient ξ (**d-f**). **a, d** $t_{th} = 0.8a$; **b, e** $t_{th} = a$, (**c, f**): $t_{th} = 1.2a$

lattice prior to failure. Figure 4a–c represents the change in S_{xxxx} for different thresholds t_{th} . Interestingly, while the number of partially failing lattices depends on the threshold, the "amount" of change in stiffness for each particular lattice does not. It is easy to observe that the stiffness change is largest closer to the center of the triangle (equi-thickness lattice). This is due to the fact that the failing beam has a larger thickness in these cases and therefore facilitates a larger contribution to the overall stiffness. As expected, the changes are always negative, i.e., S_{xxxx} becomes smaller due to failure. Finally, Fig. 4a–c shows that the change in S_{xxxx} is much larger in one of the three regions of partial failure. This is because beam 0, aligned with direction x , has the largest influence on the stiffness in this direction. In particular, Fig. 4c reveals that for $t_{th} > a$, only anisotropic lattices become viable options for damage-tolerant design with constant mass since they are able to retain a fraction of their load-bearing capacity when the isotropic equi-thickness lattice fails completely. Figure 4d–f shows the change in the anisotropy coefficient due to failure in partially failing lattices for different thresholds. Similarly to stiffness, the magnitude of the change depends on the location in the triangle, but not on the threshold. Additionally, the absolute value of the change is largest in the center of the triangle. We observe that the change is always positive, i.e., the anisotropic effects always become larger after failure. This

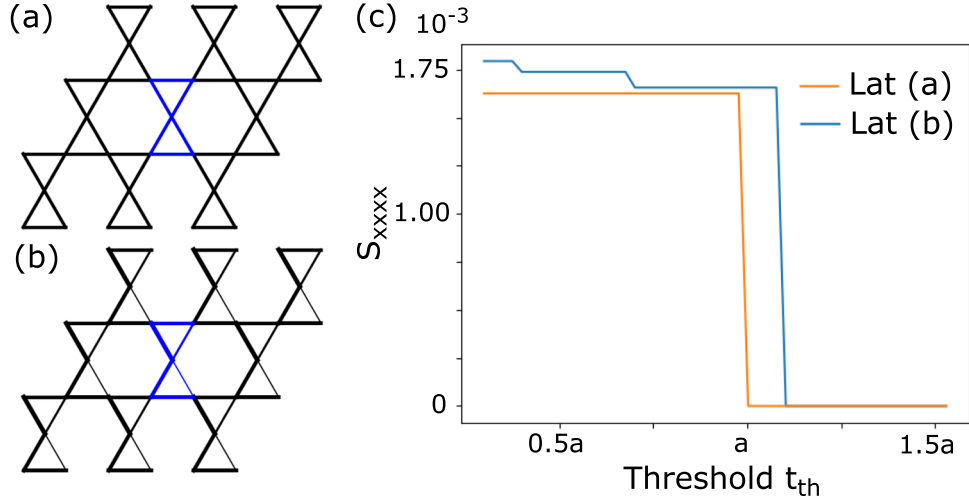


Fig. 5 Kagome lattices. **a** The kagome lattice assembled from beams of thickness a . **b** The kagome lattice assembled from beams of varying thicknesses with an average thickness of a . The blue beams highlight the simulated unit cells. **c** The stiffness S_{xxxx} of both lattices as a function of the failure threshold t_{th}

is expected since Fig. 2f has shown that the anisotropy coefficient increases with an increase in the variance of thicknesses.

To demonstrate that the proposed approach can be extended beyond triangular-based structures, we considered the kagome lattice as an example (Fig. 5). In general, a unit cell of the kagome lattice is defined by six beams. This shifts the problem from 3D space to 6D space as compared with triangular lattice if no restrictions on the total mass or average thickness are imposed. In a scenario similar to the one considered earlier, where the average thickness of the beams in the lattice is kept constant, the kagome lattice has five independent variables corresponding to the beam thicknesses. Due to the sheer number of possibilities, developing a systematic approach to cover the entire property space becomes a much more challenging problem. This might necessitate the use of more advanced techniques such as active learning [23]. However, to showcase the advantage of designs with non-equivalent beams against possible manufacturing defects, we selected a specific lattice shown in Fig. 5b and compared it with an isotropic lattice (Fig. 5a). The lattice in Fig. 5b has the same average beam thickness a but different individual beam thicknesses with a standard deviation of approximately $0.34a$, and its anisotropy coefficient is approximately 6.71×10^{-4} . A comparison between these two kagome lattices in Fig. 5c highlights two important differences. First, for relatively small failure thresholds t_{th} , these lattices exhibit similar stiffness in the x direction (S_{xxxx}), assuming the failure probability according to Eq. 4. However, lattice (b) has a slightly larger S_{xxxx} since the horizontal beams contributing most to S_{xxxx} are thicker compared to the intact lattice. According to Fig. 5c, the stiffness of lattice (a), assembled from beams of the same thickness a , drops to 0 for $t_{th} \geq a$ since all beams fail. Simultaneously, lattice (b) maintains its structural integrity beyond $t_{th} = a$ and fails completely only for $t_{th} > 1.1a$. This behavior validates the proposed concept that some anisotropic lattices might be more robust to failure due to fabrication defects as compared to their isotropic counterparts.

4 Conclusion

We propose a new perspective on anisotropic lattice materials that considers potential fabrication defects. This idea stems from the need to design lattices that are more tolerant to manufacturing imperfections, especially when operating at the minimum feature size of the chosen fabrication technique. While a classical triangular lattice made of beams with uniform thickness exhibits an isotropic response, it is not robust against the manufacturing defects discussed in this manuscript. By assuming that a probability of failure is related to the beam thickness and using a step-function approximation, we demonstrate that while the isotropic lattice fails completely, alternative anisotropic lattices with the same mass can maintain structural integrity even after partial failure. Through the use of the step function and a minimal viable unit cell defined by three beams of different thicknesses, we establish connections between the lattice's geometry, mechanical properties, and robustness.

Specifically, we illustrate that for a sufficiently large threshold value t_{th} , it is necessary to employ anisotropic designs to retain some load-bearing capacity even after partial failure, as the isotropic lattice assembled from beams of the same thickness fails completely. We encourage further exploration of this approach in more complex systems. 0

Acknowledgements Funded by the Deutsche Forschungsgemeinschaft (DFG, German Research Foundation) under Germany's Excellence Strategy—EXC-2193/1—390951807. The authors acknowledge support by the state of Baden-Württemberg through bwHPC and the German Research Foundation (DFG) through Grant No. INST 39/963-1 FUGG (bwForCluster NEMO).

Open Access This article is licensed under a Creative Commons Attribution 4.0 International License, which permits use, sharing, adaptation, distribution and reproduction in any medium or format, as long as you give appropriate credit to the original author(s) and the source, provide a link to the Creative Commons licence, and indicate if changes were made. The images or other third party material in this article are included in the article's Creative Commons licence, unless indicated otherwise in a credit line to the material. If material is not included in the article's Creative Commons licence and your intended use is not permitted by statutory regulation or exceeds the permitted use, you will need to obtain permission directly from the copyright holder. To view a copy of this licence, visit <http://creativecommons.org/licenses/by/4.0/>.

Funding Open Access funding enabled and organized by Projekt DEAL. Funding was provided by Deutsche Forschungsgemeinschaft (Grant Nos. EXC-2193/1-390951807, INST 39/963-1 FUGG (bwForCluster NEMO)).

Declarations

Conflict of interest The authors have no relevant financial or non-financial interests to disclose.

References

- Zheng, X., Lee, H., Weisgraber, T.H., Shusteff, M., DeOtte, J., Duoss, E.B., Kuntz, J.D., Biener, M.M., Ge, Q., Jackson, J.A., Kucheyev, S.O., Fang, N.X., Spadaccini, C.M.: Ultralight, ultrastiff mechanical metamaterials. *Science* **344**(6190), 1373–1377 (2014). <https://doi.org/10.1126/science.1252291>
- Jia, Z., Liu, F., Jiang, X., Wang, L.: Engineering lattice metamaterials for extreme property, programmability, and multifunctionality. *J. Appl. Phys.* **127**(15), 150901 (2020). <https://doi.org/10.1063/5.0004724>
- Montemayor, L., Chernow, V., Greer, J.R.: Materials by design: using architecture in material design to reach new property spaces. *MRS Bull.* **40**(12), 1122–1129 (2015). <https://doi.org/10.1557/mrs.2015.263>
- Yu, X., Zhou, J., Liang, H., Jiang, Z., Wu, L.: Mechanical metamaterials associated with stiffness, rigidity and compressibility: a brief review. *Prog. Mater. Sci.* **94**, 114–173 (2018). <https://doi.org/10.1016/j.pmatsci.2017.12.003>
- Bauer, J., Meza, L.R., Schaedler, T.A., Schwaiger, R., Zheng, X., Valdevit, L.: Nanolattices: an emerging class of mechanical metamaterials. *Adv. Mater.* **29**(40), 1701850 (2017). <https://doi.org/10.1002/adma.201701850>
- Benedetti, M., Plessis, A., Ritchie, R.O., Dallago, M., Razavi, N., Berto, F.: Architected cellular materials: a review on their mechanical properties towards fatigue-tolerant design and fabrication. *Mater. Sci. Eng. R. Rep.* **144**, 100606 (2021). <https://doi.org/10.1016/j.mser.2021.100606>
- Ren, X., Das, R., Tran, P., Ngo, T.D., Xie, Y.M.: Auxetic metamaterials and structures: a review. *Smart Mater. Struct.* **27**(2), 023001 (2018). <https://doi.org/10.1088/1361-665X/aaa61c>
- Felsch, G., Ghavidelnia, N., Schwarz, D., Slesarenko, V.: Controlling auxeticity in curved-beam metamaterials via a deep generative model. *Comput. Methods Appl. Mech. Eng.* **410**, 116032 (2023). <https://doi.org/10.1016/j.cma.2023.116032>
- Schwarz, D., Felsch, G., Tauber, F., Schiller, S., Slesarenko, V.: Exploiting self-contact in mechanical metamaterials for new discrete functionalities. *Mater. Des.* **236**, 112468 (2023). <https://doi.org/10.1016/j.matdes.2023.112468>
- Wu, L., Li, B., Zhou, J.: Isotropic negative thermal expansion metamaterials. *ACS Appl. Mater. Interfaces* **8**(27), 17721–17727 (2016). <https://doi.org/10.1021/acsami.6b05717>
- Milton, G.W., Cherkaev, A.V.: Which elasticity tensors are realizable? *J. Eng. Mater. Technol.* **117**(4), 483–493 (1995). <https://doi.org/10.1115/1.2804743>
- Fernandez-Corbaton, I., Rockstuhl, C., Ziemke, P., Gumbsch, P., Albiez, A., Schwaiger, R., Frenzel, T., Kadic, M., Wegener, M.: New twists of 3d chiral metamaterials. *Adv. Mater.* **31**(26), 1807742 (2019). <https://doi.org/10.1002/adma.201807742>
- Goswami, D., Zhang, Y., Liu, S., Abdalla, O.A., Zavattieri, P.D., Martinez, R.V.: Mechanical metamaterials with programmable compression-twist coupling. *Smart Mater. Struct.* **30**(1), 015005 (2020). <https://doi.org/10.1088/1361-665X/abc182>
- Ganghoffer, J.-F., Wazne, A., Reda, H.: Frontiers in homogenization methods towards generalized continua for architected materials. *Mech. Res. Commun.* **130**, 104114 (2023). <https://doi.org/10.1016/j.mechrescom.2023.104114>
- Dos Reis, F., Ganghoffer, J.F.: Equivalent mechanical properties of auxetic lattices from discrete homogenization. *Comput. Mater. Sci.* **51**(1), 314–321 (2012). <https://doi.org/10.1016/j.commatsci.2011.07.014>
- Berinskii, I.E.: Elastic in-plane properties of cellular materials: discrete approach. *Mech. Mater.* **148**, 103501 (2020). <https://doi.org/10.1016/j.mechmat.2020.103501>
- Mirzaali, M.J., Janbaz, S., Strano, M., Vergani, L., Zadpoor, A.A.: Shape-matching soft mechanical metamaterials. *Sci. Rep.* **8**(1), 965 (2018). <https://doi.org/10.1038/s41598-018-19381-3>
- Telgen, B., Sigmund, O., Kochmann, D.M.: Topology optimization of graded truss lattices based on on-the-fly homogenization. *J. Appl. Mech.* (2022). <https://doi.org/10.1115/1.4054186>

19. Estrin, Y., Beygelzimer, Y., Kulagin, R., Gumbsch, P., Fratzl, P., Zhu, Y., Hahn, H.: Architecturing materials at mesoscale: some current trends. *Mater. Res. Lett.* **9**(10), 399–421 (2021). <https://doi.org/10.1080/21663831.2021.1961908>
20. Ryvkin, M., Cherkaev, A.: Analysis of randomly damaged triangular beam lattice: elastic field and effective properties. *Math. Mech. Solids* **26**(8), 1219–1237 (2021). <https://doi.org/10.1177/10812865211021637>
21. Wilt, J.K., Yang, C., Gu, G.X.: Accelerating auxetic metamaterial design with deep learning. *Adv. Eng. Mater.* **22**(5), 1901266 (2020). <https://doi.org/10.1002/adem.201901266>
22. Yu, G., Xiao, L., Song, W.: Deep learning-based heterogeneous strategy for customizing responses of lattice structures. *Int. J. Mech. Sci.* **229**, 107531 (2022). <https://doi.org/10.1016/j.ijmecsci.2022.107531>
23. Kulagin, R., Reiser, P., Truskovskiy, K., Koeppe, A., Beygelzimer, Y., Estrin, Y., Friederich, P., Gumbsch, P.: Lattice metamaterials with mesoscale motifs: exploration of property charts by Bayesian optimization. *Adv. Eng. Mater.* **25**, 2300048 (2023). <https://doi.org/10.1002/adem.202300048>
24. Shu, X., Mao, Y., Lei, M., Da, D., Hou, S., Zhang, P.: Toughness enhancement of honeycomb lattice structures through heterogeneous design. *Mater. Des.* **217**, 110604 (2022). <https://doi.org/10.1016/j.matdes.2022.110604>
25. Meza, L.R., Zelhofer, A.J., Clarke, N., Mateos, A.J., Kochmann, D.M., Greer, J.R.: Resilient 3d hierarchical architected metamaterials. *Proc. Natl. Acad. Sci.* **112**(37), 11502–11507 (2015). <https://doi.org/10.1073/pnas.1509120112>
26. Alberdi, R., Dingreville, R., Robbins, J., Walsh, T., White, B.C., Jared, B., Boyce, B.L.: Multi-morphology lattices lead to improved plastic energy absorption. *Mater. Des.* **194**, 108883 (2020). <https://doi.org/10.1016/j.matdes.2020.108883>
27. Pham, M.-S., Liu, C., Todd, I., Lertthanasarn, J.: Damage-tolerant architected materials inspired by crystal microstructure. *Nature* **565**(7739), 305–311 (2019). <https://doi.org/10.1038/s41586-018-0850-3>
28. Ryvkin, M., Slesarenko, V., Cherkaev, A., Rudykh, S.: Fault-tolerant elastic–plastic lattice material. *Philos. Trans. R. Soc. A Math. Phys. Eng. Sci.* **378**(2162), 20190107 (2020). <https://doi.org/10.1098/rsta.2019.0107>
29. Kadic, M., Bückmann, T., Stenger, N., Thiel, M., Wegener, M.: On the practicability of pentamode mechanical metamaterials. *Appl. Phys. Lett.* (2012). <https://doi.org/10.1063/1.4709436>
30. Bauer, J., Schroer, A., Schwaiger, R., Kraft, O.: Approaching theoretical strength in glassy carbon nanolattices. *Nat. Mater.* **15**(4), 438–443 (2016). <https://doi.org/10.1038/nmat4561>
31. Askari, M., Hutchins, D.A., Thomas, P.J., Astolfi, L., Watson, R.L., Abdi, M., Ricci, M., Laureti, S., Nie, L., Freear, S., Wildman, R., Tuck, C., Clarke, M., Woods, E., Clare, A.T.: Additive manufacturing of metamaterials: a review. *Addit. Manuf.* **36**, 101562 (2020). <https://doi.org/10.1016/j.addma.2020.101562>
32. Nazir, A., Gokcekaya, O., Masum Billah, K., Ertugrul, O., Jiang, J., Sun, J., Hussain, S.: Multi-material additive manufacturing: a systematic review of design, properties, applications, challenges, and 3d printing of materials and cellular metamaterials. *Mater. Des.* **226**, 111661 (2023). <https://doi.org/10.1016/j.matdes.2023.111661>
33. Corvi, A., Collini, L., Sciancalepore, C., Kumar, A.: Analysis and modelling of damage mechanism in FDM 3d-printed lattice structure under compression loading. *J. Mech. Sci. Technol.* **37**(3), 1089–1095 (2023). <https://doi.org/10.1007/s12206-022-2104-4>
34. Mohsenizadeh, M., Gasbarri, F., Munther, M., Beheshti, A., Davami, K.: Additively-manufactured lightweight metamaterials for energy absorption. *Mater. Des.* **139**, 521–530 (2018). <https://doi.org/10.1016/j.matdes.2017.11.037>
35. Eckel, Z.C., Zhou, C., Martin, J.H., Jacobsen, A.J., Carter, W.B., Schaedler, T.A.: Additive manufacturing of polymer-derived ceramics. *Science* **351**(6268), 58–62 (2016). <https://doi.org/10.1126/science.aad2688>
36. Valdevit, L., Bauer, J.: Chapter 13.1—fabrication of 3d micro-architected/nano-architected materials. In: Baldacchini, T. (ed.) *Three-Dimensional Microfabrication Using Two-Photon Polymerization*. Micro and Nano Technologies, pp. 345–373. William Andrew Publishing, New York (2016)
37. Plessis, A., Razavi, N., Benedetti, M., Murchio, S., Leary, M., Watson, M., Bhate, D., Berto, F.: Properties and applications of additively manufactured metallic cellular materials: a review. *Prog. Mater. Sci.* **125**, 100918 (2022). <https://doi.org/10.1016/j.pmatsci.2021.100918>
38. Glaesener, R.N., Kumar, S., Lestringant, C., Butruille, T., Portela, C.M., Kochmann, D.M.: Predicting the influence of geometric imperfections on the mechanical response of 2d and 3d periodic trusses. *Acta Mater.* **254**, 118918 (2023). <https://doi.org/10.1016/j.actamat.2023.118918>
39. François, M.L., Chen, L., Coret, M.: Elasticity and symmetry of triangular lattice materials. *Int. J. Solids Struct.* **129**, 18–27 (2017). <https://doi.org/10.1016/j.ijsolstr.2017.09.019>
40. Khakalo, S., Niiranen, J.: Lattice structures as thermoelastic strain gradient metamaterials: evidence from full-field simulations and applications to functionally step-wise-graded beams. *Compos. B Eng.* **177**, 107224 (2019). <https://doi.org/10.1016/j.compositesb.2019.107224>
41. Rosi, G., Auffray, N.: Continuum modelling of frequency dependent acoustic beam focussing and steering in hexagonal lattices. *Eur. J. Mech. A. Solids* **77**, 103803 (2019). <https://doi.org/10.1016/j.euromechsol.2019.103803>
42. Yang, H., Timofeev, D., Giorgio, I., Müller, W.H.: Effective strain gradient continuum model of metamaterials and size effects analysis. *Contin. Mech. Thermodyn.* **35**(3), 775–797 (2023). <https://doi.org/10.1007/s00161-020-00910-3>
43. Aage, N., Andreassen, E., Lazarov, B.S., Sigmund, O.: Giga-voxel computational morphogenesis for structural design. *Nature* **550**(7674), 84–86 (2017). <https://doi.org/10.1038/nature23911>
44. Xia, L., Fritzen, F., Breitkopf, P.: Evolutionary topology optimization of elastoplastic structures. *Struct. Multidiscip. Optim.* **55**, 569–581 (2017). <https://doi.org/10.1007/s00158-016-1523-1>
45. Harper, M.: python-ternary: ternary plots in python. Zenodo. <https://doi.org/10.5281/zenodo.594435>
46. Karathanasopoulos, N., Dos Reis, F., Hadjidoukas, P., Ganghoffer, J.-F.: Latticemach: a discrete mechanics code to compute the effective static properties of 2d metamaterial structures. *SoftwareX* **11**, 100446 (2020). <https://doi.org/10.1016/j.softx.2020.100446>
47. Dos Reis, F., Ganghoffer, J.: Equivalent mechanical properties of auxetic lattices from discrete homogenization. *Comput. Mater. Sci.* **51**(1), 314–321 (2012). <https://doi.org/10.1016/j.commatsci.2011.07.014>
48. Karathanasopoulos, N., Dos Reis, F., Reda, H., Ganghoffer, J.-F.: Computing the effective bulk and normal to shear properties of common two-dimensional architected materials. *Comput. Mater. Sci.* **154**, 284–294 (2018). <https://doi.org/10.1016/j.commatsci.2018.07.044>

49. Zener, C.: Contributions to the theory of beta-phase alloys. *Phys. Rev.* **71**(12), 846–851 (1947). <https://doi.org/10.1103/PhysRev.71.846>
50. Li, Z., Bradt, R.C.: The single-crystal elastic constants of cubic (3c) sic to 1000 c. *J. Mater. Sci.* **22**, 2557–2559 (1987). <https://doi.org/10.1007/BF01082145>
51. Ranganathan, S.I., Ostoja-Starzewski, M.: Universal elastic anisotropy index. *Phys. Rev. Lett.* **101**(5), 055504 (2008). <https://doi.org/10.1103/PhysRevLett.101.055504>
52. Li, R., Shao, Q., Gao, E., Liu, Z.: Elastic anisotropy measure for two-dimensional crystals. *Extreme Mech. Lett.* **34**, 100615 (2020). <https://doi.org/10.1016/j.eml.2019.100615>
53. Méndez, C., Podestá, J., Toro, S., Huespe, A.E., Oliver, J.: Making use of symmetries in the three-dimensional elastic inverse homogenization problem. *Int. J. Multiscale Comput. Eng.* (2019). <https://doi.org/10.1615/IntJMultCompEng.2019029111>

Publisher's Note Springer Nature remains neutral with regard to jurisdictional claims in published maps and institutional affiliations.